Proton-production double-differential cross sections for 300-MeV and 392-MeV proton-induced reactions

Hiroki Iwamoto,[1,2] Minoru Imamura,[1] Yusuke Koba,[1] Yoshinori Fukui,[1] Genichiro Wakabayashi,[1] Yusuke Uozumi,[1,*] Tadahiro Kin,[2] Yosuke Iwamoto,[2] Shinya Hohara,[3] and Masahiro Nakano[4]

[1]*Department of Applied Quantum Physics and Nuclear Engineering, Kyushu University, 744 Motooka, Nishi-ku, Fukuoka 819-0395, Japan*

[2]*Japan Atomic Energy Agency, Tokai-mura, Naka-gun, Ibaraki 319-1195, Japan*

[3]*Kinki University Atomic Energy Research Institute, Kowakae, Higashiosaka 577-8502, Japan*

[4]*University of Occupational and Environmental Health, Kitakyushu 807-8555, Japan*

(Received 15 February 2009; published 13 September 2010)

We investigate proton-production double-differential cross sections (DDXs) for 300- and 392-MeV proton-induced reactions on O, V, Tb, Ta, Au, Pb, and Bi. Emitted proton energies are measured with stacked scintillator spectrometers by the $\Delta E - E$ technique. Experimental results are compared with the intranuclear cascade (INC) and quantum molecular dynamics models. Although both models can reproduce spectral DDXs, there is a difference at the most forward and backward angles. The cause of these differences is discussed in terms of the refraction caused by the nuclear potential. Angular distributions of the present data are well accounted for by the Kalbach systematics plus INC one-step calculations. The quasi-free-scattering contribution increases with decreasing target mass and increasing emission energy.

DOI: 10.1103/PhysRevC.82.034604 PACS number(s): 25.40.Ep, 25.40.Sc, 29.40.Mc

I. INTRODUCTION

Proton-production cross sections at intermediate energies have received renewed interest in recent years in the attempt to understand bulk nuclear reactions. They attract particular attention in obtaining the nuclear data needed for many applications. For instance, the design of spallation neutron sources used in basic neutron sciences and accelerator-driven systems (ADSs) of the transmutation of nuclear wastes requires a reliable estimation of secondary particle transportation, radiation heating, and radiation damage of materials. Furthermore, nuclear data are used for estimation of radiation dose and malfunction of a microelectronic device during space missions. To meet these engineering requirements, absolute double-differential cross section (DDX) data is indispensable for quantitative predictions.

Much effort has been devoted to understanding bulk nuclear reactions at the intermediate energy [1,2]. In recent years, Ginger *et al.* [3] carried out an intensive study with the ISiS array. They obtained exclusive correlation data in addition to inclusive data. On the basis of serious theoretical data analyses, they concluded that nonequilibrium particle emission comes from a localized region in the early stage of the energy-dissipation process. This result provided us with essential insight into the mechanism of bulk nuclear reactions. However, both their theoretical and their experimental research was qualitative. Although quantitative results are necessary for engineering purposes, the predictive abilities of the theoretical calculations have not been verified for even the early-stage process.

We have started an experimental study of DDXs of proton production from proton-nucleus reactions in the energy region from 300 to 400 MeV. So far, we have investigated DDXs of (p, xp') reactions on ^{12}C, ^{27}Al, and ^{93}Nb at beam energies of 300 and 392 MeV [4]. The data were compared with two theoretical calculations, intranuclear cascade (INC) and quantum molecular dynamics (QMD) [5,6], and demonstrated that the use of more realistic ground-state parameters leads to better accounts of cross sections on these light- and medium-weight nuclei. There are many heavier elements for which measurements are required for nuclear data. It is important to measure cross sections and validate theoretical calculations for heavy nuclei.

In the present article, (p,xp') cross sections are investigated on Au, Pb, and Bi using 300- and 392-MeV proton beams. Two of the targets, Pb and Bi, are chosen because they are expected to be used as the target and/or coolant in ADSs and as radiation shield materials in many different applications. Measurements for these targets are made at a beam energy of 392 MeV. Gold was chosen because it is used in large-scale integrations, and the estimation of secondary particle productions is important during space missions. Moreover, continua of ^{197}Au(p,xp') reactions have been studied extensively below a beam energy of 200 MeV [7]. Experimental data obtained at higher energies are essential for a systematic understanding of this reaction. Hence, the measurements for gold are conducted at 300 and 392 MeV. The present data are compared with the INC and QMD calculations. The applicability of these models to heavy elements is discussed. In addition to heavy nuclear targets, we investigate cross sections for lighter targets to cover the periodic table at shorter intervals. To this end, we have chosen oxygen, vanadium, terbium, and tantalum. Spectral DDXs of reactions at 300 to 400 MeV help to elucidate the mechanism of the cascade process for theoretical improvements, as the nuclear potential is weak, the incident particle can penetrate deep into the target nucleus, and the Δ degrees of freedom are negligible in this energy domain.

*uozumi@nucl.kyushu-u.ac.jp

The angular distributions obtained here are also investigated in terms of the multistep direct reaction component and the quasifree knockout component on the basis of Kalbach systematics [8]. The energy differential cross sections of the multistep direct component are extracted using the Kalbach's prescription, and their target mass dependences are discussed.

The present paper is organized as follows. In Sec. II, we describe the experimental setup and the data analysis. In Sec. III, we briefly present the INC and QMD models. In Sec. IV, the experimental results are compared with the theoretical models. Finally, conclusions are presented in Sec. V.

II. EXPERIMENT AND DATA REDUCTION

Because a detailed description of the experiment is given in Ref. [4], only a brief explanation is provided here. The experiment was carried out at the Research Center for Nuclear Physics (RCNP), Osaka University. The experimental setup is schematized in Fig. 1. Self-supporting targets were bombarded with 300- and 392-MeV proton beams with a beam current of approximately 5 nA from the ring cyclotron at the RCNP. The beam spot was smaller than 5 mm in diameter and centered on the target within 0.5 mm. The beam current was measured with a Faraday cup located about 4 m downstream from the target position.

The targets used in this experiment and their thicknesses are reported in Table I. Purities of ^{208}Pb and ^{209}Bi were 98% and 97%, respectively. The proton scattering off hydrogen contained in polyester was used in energy calibration of the scintillators. Emitted proton energies were measured by stacked scintillator spectrometers. The spectrometers were $\Delta E - E$ counter telescopes consisting of three plastic scintillators and three GSO(Ce) crystals connected with photomultiplier tubes. As described in Ref. [4], we used two different types of GSO(Ce) crystals (see Fig. 1). The long one consisted of two

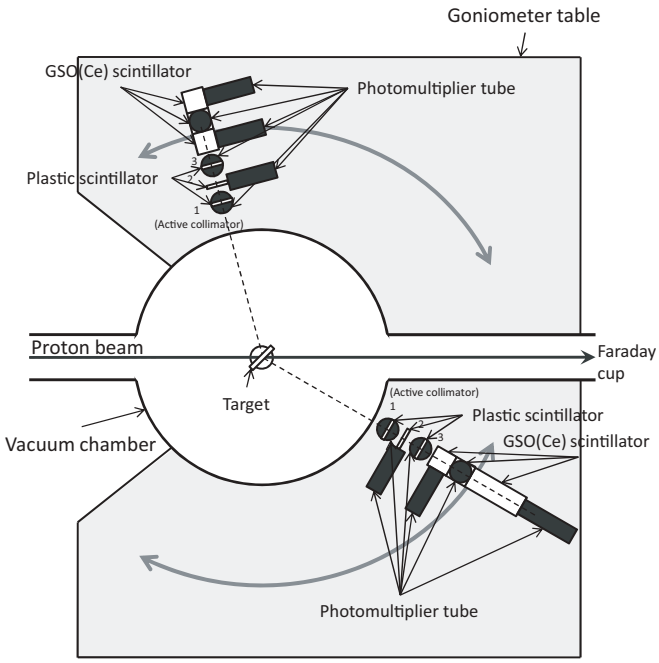

FIG. 1. Schematic of the experimental setup.

TABLE I. Target thickness used in this experiment.

Incident energy	Target	Thickness (mg/cm^2)
300 MeV	Al_2O_3	1.34
	^{nat}Au	19.32
392 MeV	^{nat}V	2.54
	^{nat}Tb	2.24
	^{nat}Ta	4.07
	^{nat}Au	19.32
	^{208}Pb	9.93
	^{209}Bi	0.49

cubic and one cylindrical GSO(Ce) crystals. The cubic crystals measured 43 mm on a side. The cylindrical crystal was 60 mm in diameter and 120 mm in length. The short one comprised three cubic GSO(Ce) crystals. The first plastic scintillator was used as an active slit, a 5-mm-thick, 50 × 50-mm square plate with a 15-mm-diameter circular opening at its center. The solid angle of the active slit was 0.84 mSr. The two plastic scintillators placed after the first scintillator and before the GSO(Ce) crystals of each spectrometer served as ΔE detectors. These plates were 1 and 2 mm thick, respectively.

The spectrometers were installed on a goniometer table outside the vacuum chamber. They were positioned on opposite sides of the beam axis in the same reaction plane. The short spectrometer was located at 105°, while the long one was placed at some other forward angle. Deposited proton energies were obtained by performing energy calibrations. Here, the GSO(Ce) crystals took into account the light output nonlinearity [9].

To determine the absolute cross sections, the integrated beam current was measured during each run using a Faraday cup current integrator assembly combined with a CAMAC scaler system, whose accuracy has been evaluated within 5%. Background owing to beam halo, which could distort energy distributions, was measured several times using a empty target frame. The background events were found to be protons of energies below 50 MeV. Their contribution to the DDXs was about 1% at an outgoing energy of 40 MeV and negligible at higher energies. Therefore, we made no corrections for the background protons.

The DDXs were determined using the following equation:

$$\frac{d^2\sigma}{d\Omega\, d\varepsilon} = \frac{Y}{P S_t \phi \Delta\Omega \Delta\varepsilon}, \tag{1}$$

where $\Delta\varepsilon$ and $\Delta\Omega$ are the bin size of the energy and the solid angle of the spectrometers, respectively. P is the peak efficiency of the spectrometer, which was investigated as a function of energy up to 400 MeV [10]. S_t is the surface density of the targets, ϕ is the number of incident protons, and Y is the proton yield per $\Delta\varepsilon$ at the detection angle of interest.

The yield Y was determined as follows. To identify protons, the particle identification quantity (PI) technique was employed. The PI is given by

$$\mathrm{PI} = E_{\mathrm{tot}}^{b} - (E_{\mathrm{tot}} - \Delta E)^{b}, \tag{2}$$

where E_{tot} is the proton total energy deposited in the spectrometer, which is equivalent to the emitted proton energy

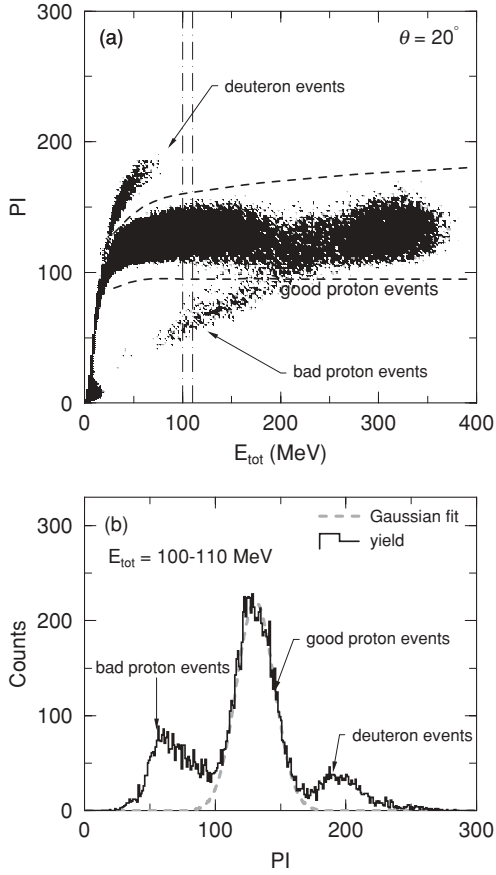

FIG. 2. (a) Two-dimensional plot of PI versus $E_{\rm tot}$ obtained at 20° for the 392-MeV ^{181}Ta(p,xp') reaction. (b) PI distribution for $E_{\rm tot}$ = 100–110 MeV indicated by dot-dashed lines in (a). The dashed line in (b) shows a Gaussian fit, and the dashed lines in (a) correspond to $\pm 3\sigma$ deviation of the resultant Gaussians.

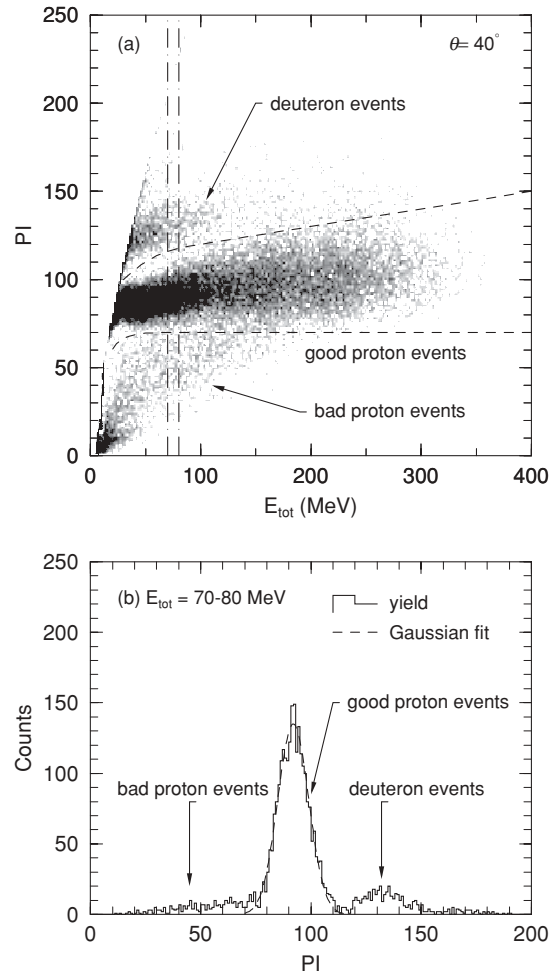

FIG. 3. (a) Two-dimensional plot of PI versus $E_{\rm tot}$ obtained at 40° for the 392-MeV ^{208}Pb(p,xp') reaction. (b) PI distribution for $E_{\rm tot}$ = 70–80 MeV indicated by dot-dashed lines in (a). The dashed line in (b) shows a Gaussian fit, and the dashed lines in (a) correspond to $\pm 3\sigma$ deviation of the resultant Gaussians.

from the reactions, ΔE is the proton energy deposited in the ΔE detectors, and b denotes the range of each particle. In this analysis, a b value of 1.73 was employed to obtain the best separation and extraction of a good proton event [11]. As an example, a two-dimensional plot of PI versus $E_{\rm tot}$ at 20° for the 392-MeV proton-induced reaction on ^{181}Ta is shown in Fig. 2(a). Here, the thick belt lying around PI = 130 is a good proton event, which stopped in the spectrometer through electronic interaction. Finally, the proton yield Y was obtained by fitting the histograms with a Gaussian for each energy bin of $E_{\rm tot}$. Figure 2(b) shows the particle yield and the fit at $E_{\rm tot}$ = 105 MeV for Fig. 2(a), where $\Delta\varepsilon$ = 10 MeV (100–110 MeV) was used. Another example of a PI plot is shown in Fig. 3 for the 392-MeV reaction, as in the case of Fig. 2.

III. THEORETICAL MODELS

In the present study, the predictive capabilities of the INC and the QMD model were examined. These are the two most powerful tools in the intermediate-energy region. Although there are many INC codes [12–16], we used the code that was developed and demonstrated to exhibit a high predictive power in our previous work [4]. QMD calculations were performed by the JQMD model [6] incorporated in the heavy-ion transport code system PHITS [17]. In this section, we briefly describe the ingredients of the INC and QMD models.

A. Intranuclear cascade model

The code is written within the simple frame of the time-dependent INC model. As an initial calculation condition, the position and the momentum of each nucleon in the target nucleus are determined stochastically according to the Woods-Saxon-type density [18] and the degenerate Fermi distribution, respectively. The time evolution of the nucleon position is described by relativistic kinematics by a time step of 1 fm/c. All nucleons are assumed to move in a straight line in the nuclear potential of a −45-MeV-deep square-shaped well. It is also assumed that two particles have a chance to undergo elastic scattering with each other when they fulfill the condition

$$d_{ij} \leqslant \sqrt{\frac{\sigma_{\rm tot}}{\pi}}, \tag{3}$$

where d_{ij} is the relative distance between the ith and the jth nucleons, and $\sigma_{\rm tot}$ the NN total cross section ($\sigma_{\rm tot} = \sigma_{\rm el} + \sigma_{\rm inel}$). In the present calculation, we use the parametrization of Cugnon *et al.* [19] for the NN cross section and the angular distribution of NN scattering. However, if the final state is Pauli blocked, the scattering might be prohibited. In the present calculation, we adopt the following simple form for the Pauli-blocking probability:

$$P = 1 - [1 - \Theta(p'_i - p_{\rm F})][1 - \Theta(p'_j - p_{\rm F})], \tag{4}$$

where p'_i and $p_{\rm F}$ are the momentum of the nucleon after collision and the Fermi momentum, respectively. Θ denotes the Heaviside function.

B. Quantum molecular dynamics model

Each nucleon labeled with the subscript i is assumed to be a Gaussian wave packet in the phase space in the following way:

$$f_i(\mathbf{r}, \mathbf{p}) = 8 \exp\left[-\frac{(\mathbf{r} - \mathbf{R}_i)^2}{4L} - \frac{2L(\mathbf{p} - \mathbf{P}_i)^2}{\hbar^2}\right], \tag{5}$$

$$f(\mathbf{r}, \mathbf{p}) = \sum_i f_i(\mathbf{r}, \mathbf{p}), \tag{6}$$

where L is a parameter representing the spatial spread of a wave packet. $\mathbf{R}_i$ and $\mathbf{P}_i$ are the centers of a wave packet in the coordinate and momentum spaces, respectively. $f(\mathbf{r}, \mathbf{p})$ is the total wave function assumed to be a direct product of the Gaussian wave functions. The equation of motion of $\mathbf{R}_i$ and $\mathbf{P}_i$ is expressed as

$$\dot{\mathbf{R}}_i = \frac{\partial H}{\partial \mathbf{P}_i}, \quad \dot{\mathbf{P}}_i = -\frac{\partial H}{\partial \mathbf{R}_i}, \tag{7}$$

where the Hamiltonian has a kinetic energy term and an effective potential term:

$$H = \sum_i \sqrt{m_i^2 + \mathbf{P}_i^2} + V, \tag{8}$$

where m_i is the mass of the ith nucleon. V is given by Eq. (3) in Ref. [6]. In addition to Eq. (7), two-body NN collisions are taken into account for the time evolution of the system. The cross sections and the angular distributions of NN collisions are calculated in the same manner as in the present INC model. Pauli blocking is taken into consideration using the blocking factor $[1 - f(\mathbf{r}, \mathbf{p}, t)]$.

IV. RESULTS AND DISCUSSION

A. Energy distribution

Figures 4–7 show the obtained proton-production DDXs for O, V, Nb, Tb, Ta, Pb, and Bi targets bombarded by protons, together with the INC and QMD model calculations. The error bars show only the statistical uncertainty. Comparing the proton-hydrogen scattering measured for a polyester target with well-established values using a polyester target, we estimated the systematic errors in absolute cross sections to be 20%. The uncertainties in the relative cross sections within each spectrum and in the relative cross sections at a given angle are essentially statistical except for the energy regions corresponding to the dead layer between crystals. Overall, the spectra are characterized by a high-energy portion whose intensity decreases sharply with increasing angle. Broad peaks, which could be indicative of quasifree proton-nucleon scattering, are significant at 20° for all targets.

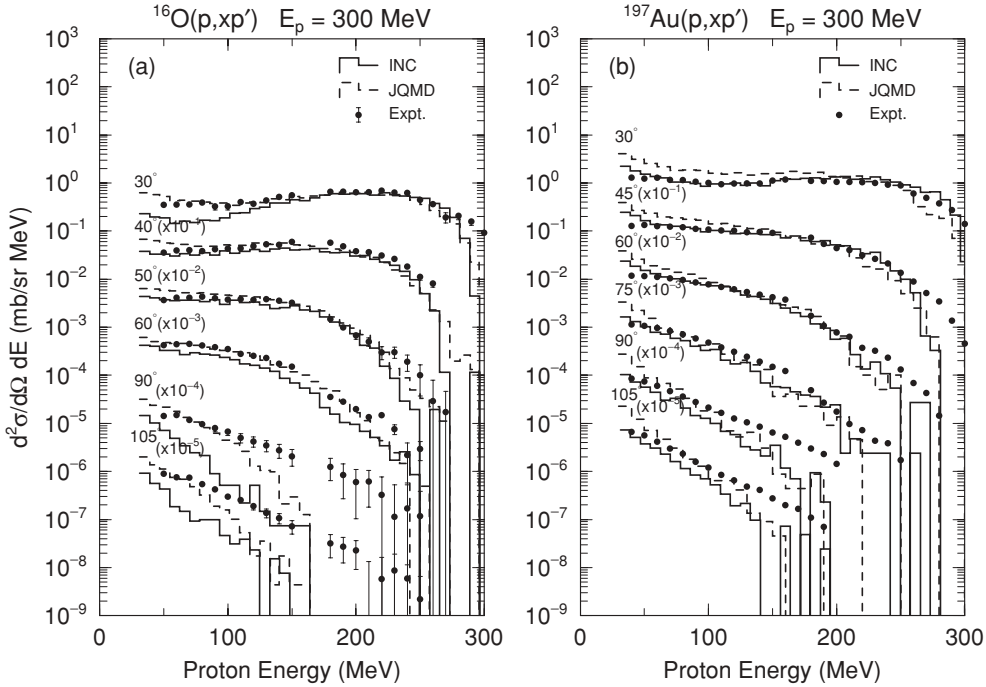

FIG. 4. Double-differential cross sections for the (p,xp') reactions on (a) ^{16}O and (b) ^{197}Au at an incident energy of 300 MeV. Results are multiplied by the indicated factors for display.

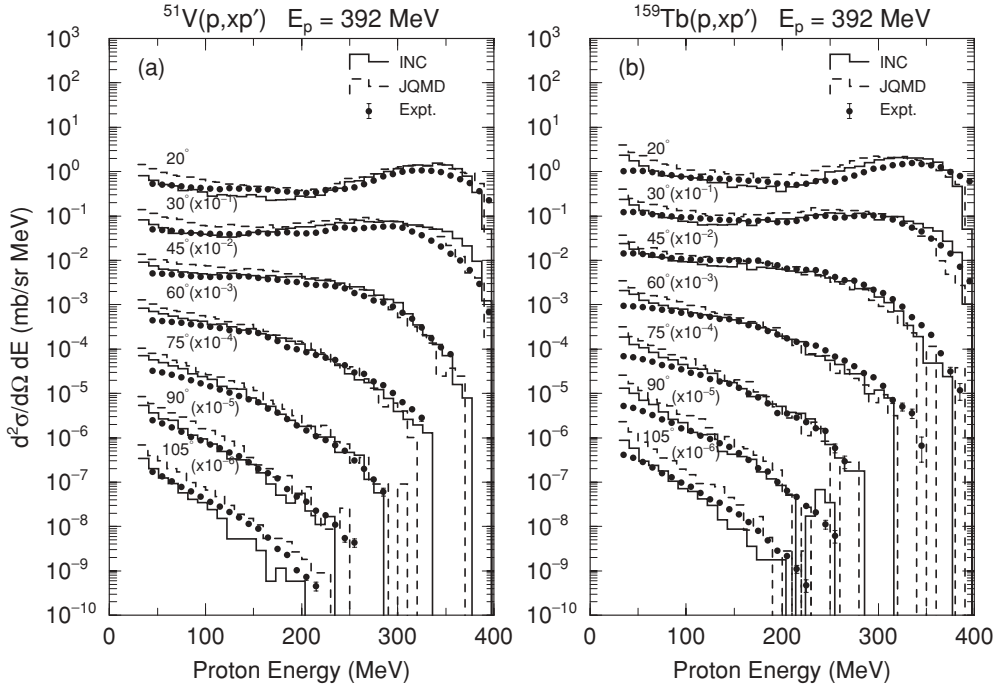

FIG. 5. Same as Fig. 2, but on (a) ^{51}V and (b) ^{159}Tb at an incident energy of 392 MeV.

The calculation results for the INC and QMD models are also shown in Fig. 4–7, by solid and dashed histograms. To date, the only calculations that seem appropriate for the intermediate-energy region are INC and QMD calculations. Both calculations are found to reproduce many of the typical features of the proton spectra and are in reasonable agreement with the measured shape of the spectra. However, it can be seen that the QMD calculation predicts too prominent a low-energy portion in the spectra at all angles. As discussed in Ref. [20], for example, QMD tends to predict higher proton spectra than INC at most forward and backward angles. It appears that QMD overestimates the spectra, especially at 20°. The INC fits are better than QMD over a wide range of proton emission energies for the angular range between 20° and 105°

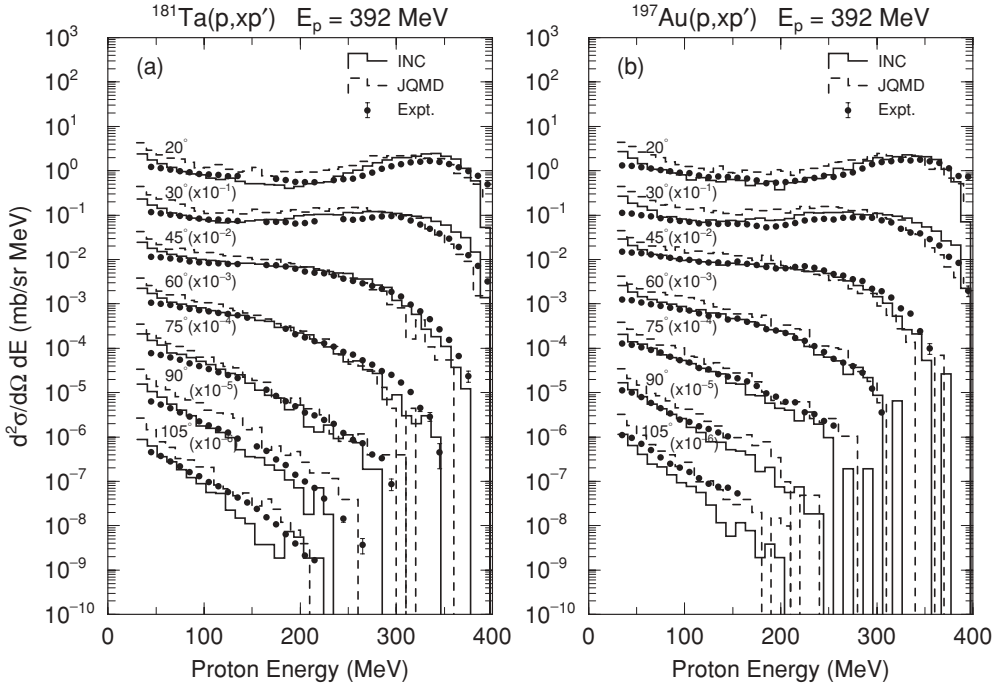

FIG. 6. Same as Fig. 2, but on (a) ^{181}Ta and (b) ^{197}Au at an incident energy of 392 MeV.

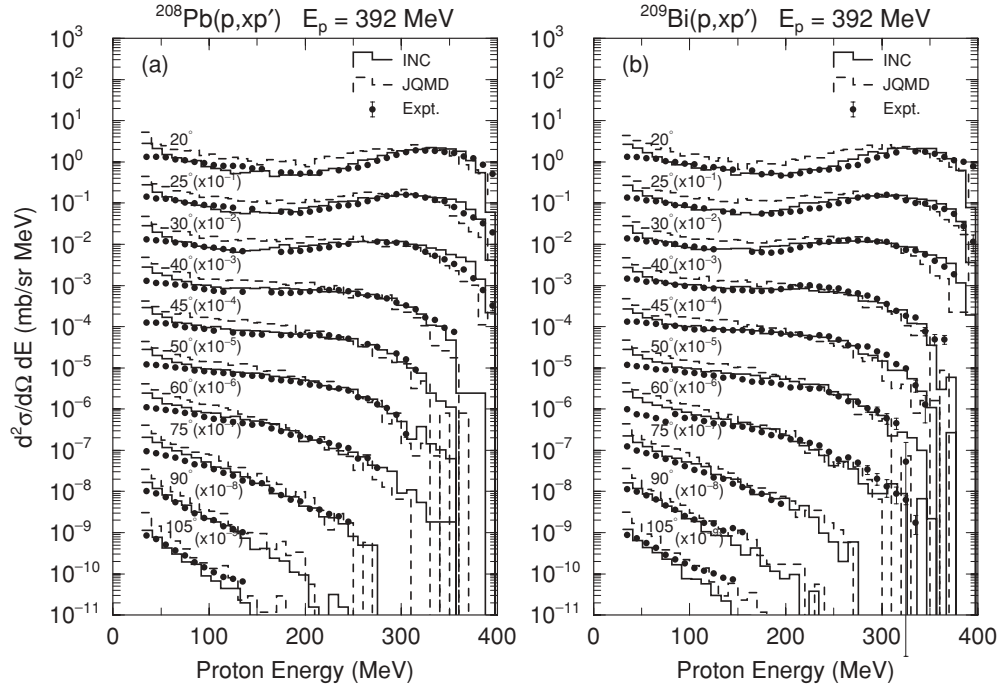

FIG. 7. Same as Fig. 2, but on (a) ^{208}Pb and (b) ^{209}Bi at an incident energy of 392 MeV.

for all targets except ^{16}O. In the case of the lightest target, ^{16}O, INC predictions are much smaller than measurements in the middle- to lower-energy regions at 20° and 105°. Meanwhile, QMD gives better predictions for ^{16}O. Because a scattered nucleon from a single NN collision cannot access this region for kinematical reasons, it might be refracted by the nuclear potential of the QMD, as discussed in Ref. [20].

An explicit explanation of the QMD refraction is given by showing nucleon trajectories in QMD calculations for the 300-MeV proton + ^{16}O reaction. Figure 8 shows typical trajectories of scattered nucleons. It can be seen that nucleons having a relatively high energy travel along an almost-straight

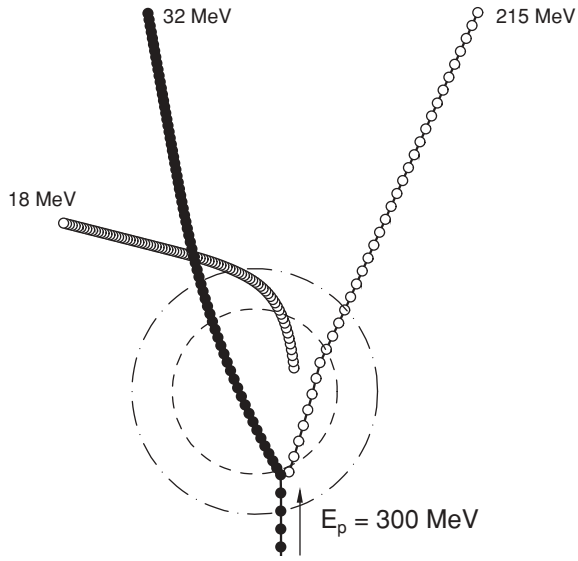

FIG. 8. Trajectories of nucleons in QMD calculations for the proton-^{16}O reaction at 300 MeV. Trajectories indicated by filled and open circles are an incident proton and scattered nucleons in the target nucleus, respectively. Dashed and dot-dashed circles indicate a nuclear radius of $r = 1.2 \times 16^{1/3}$ fm and a radius of $r = 4.5$ fm at a density of roughly $\rho(r) = 0.1\rho_0$, respectively. ρ_0 is the saturated nuclear density.

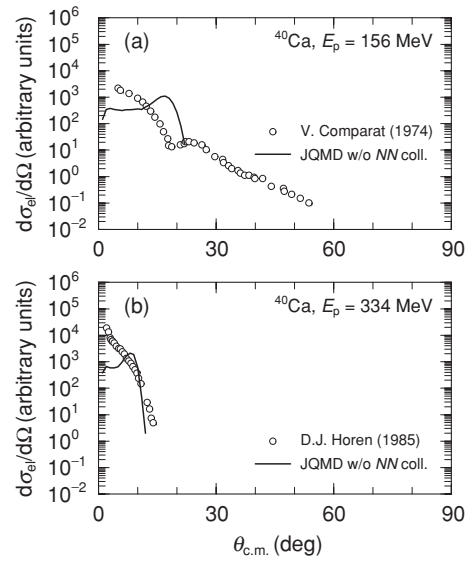

FIG. 9. Angular distributions of protons refracted off ^{40}Ca at incident energies of 156 (a) and 334 MeV (b). Solid lines denote QMD results obtained by calculating the equation of motion [Eq. (7)] without the NN collision term. Experimental data (circles) are taken from Refs. [21] and [22].

trajectory. By contrast, nucleons scattered to lower energies are strongly refracted by the nuclear potential in the surface region.

To investigate the strength of QMD refractions, the angular distribution of the refraction of QMD was calculated by ignoring the NN collisions inside the nucleus and compared with measured angular distributions of elastic scattering in Fig. 9. It should be noted that we did not check whether or not the final state of the target nucleus was excited. The QMD refraction shows a different angular distribution shape than the experimental elastic scattering [21,22]; it underestimates small- and large-angle scattering. QMD might be underpredicting the 105° data of (p, xp') reactions because of a failure in the large-angle refraction, which is attributable to the interference in wave dynamics.

B. Angular distribution

Angular distributions of the data measured in the present study were analyzed using Kalbach systematics. In Ref. [8], it was demonstrated that Kalbach systematics successfully gives the shape of the angular distributions of the pre-equilibrium component for inclusive reactions up to several hundred mega–electron volts. This systematics comprises two processes: a multistep compound (MSC) process and a multistep direct (MSD) process. However, the MSC component is negligible for the emission energy range investigated in this work. In addition, we should note that the QFS contribution is not considered in Kalbach systematics, although QFS becomes increasingly important above an incident energy of several hundred mega–electron volts. Thus, the QFS component is

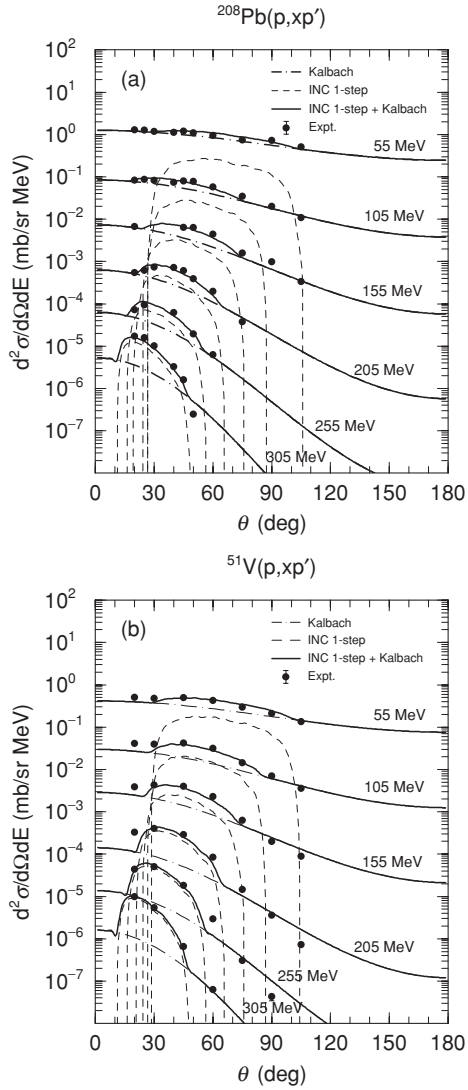

FIG. 10. Results of fitting (a) the ^{208}Pb(p,xp') and the (b) ^{51}V(p,xp') reactions at an incident energy of 392 MeV. Dot-dashed lines present the contribution of MSD with the Kalbach systematics, and dashed lines show that of QFS performed with the INC one-step calculation. Solid lines show the sum of these two contributions.

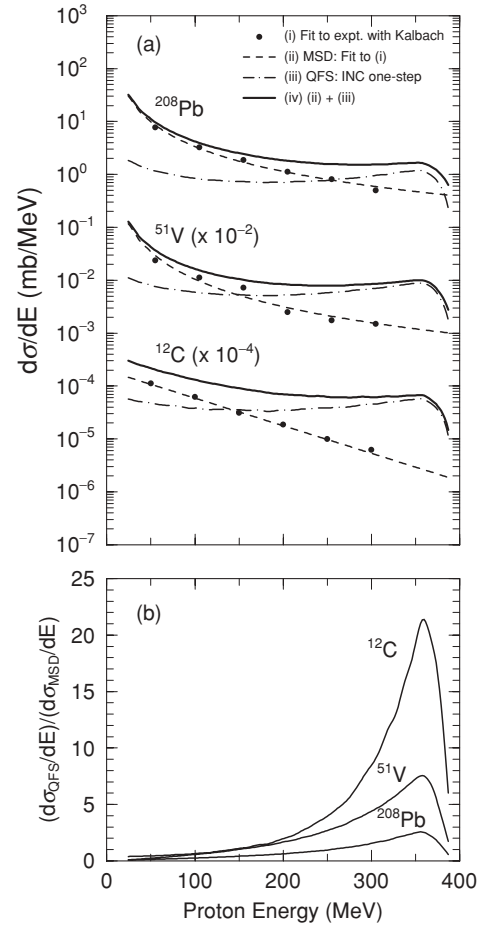

FIG. 11. (a) Angle-integrated cross sections for 392-MeV protons on ^{12}C, ^{51}V, and ^{208}Pb. Filled circles represent the results obtained from the fit with Kalbach systematics. Dashed lines show the results of fitting the filled circles (power-law fit for ^{51}V and ^{208}Pb and exponential fit for ^{12}C). Dot-dashed lines are the QFS contributions obtained from the INC one-step calculation. Solid lines depict the sum of these two lines. (b) Ratio of the angle-integrated cross section of the QFS contributions to that of the MSD contributions as a function of emitted proton energy. Displayed curves show ^{12}C(p,xp'), ^{51}V(p,xp'), and ^{208}Pb(p,xp') reactions at an incident energy of 392 MeV. The ^{12}C(p,xp') reaction is taken from Ref. [4].

incoherently added to the MSD component via the following equation:

$$\frac{d^2\sigma}{d\Omega\, dE} = \frac{d^2\sigma_{\rm QFS}}{d\Omega\, dE} + \frac{d^2\sigma_{\rm MSD}}{d\Omega\, dE}. \quad (9)$$

For example, in Ref. [23], the QFS cross section was calculated using the distorted-wave impulse approximation [24]. In principle, the INC one-step process is presumed to correspond to QFS and would be applicable to a wide range of reactions. In addition, as shown in Fig. 4, it was found that our INC model reproduced the proton spectra quite well. Thus, we calculated $d\sigma_{\rm QFS}/dE$ in Eq. (9) by performing the INC one-step calculation using our INC model, then performed a fit to the experimental MSD component.

The form for the MSD part of the angular distributions is given by [8]

$$\frac{d^2\sigma_{\rm MSD}}{d\Omega\, dE} = \frac{1}{4\pi}\frac{d\sigma_{\rm MSD}}{dE}\frac{2a}{e^a - e^{-a}}\exp(a\cos\theta), \quad (10)$$

where θ is the emission angle, $d\sigma_{\rm MSD}/dE$ is presumed to be the angle-integrated cross-section, and a denotes the slope parameter [8] as a function of the ratio of emission energy to incident energy. In this analysis, the angle-integrated cross section $d\sigma_{\rm MSD}/dE$ was a free parameter to fit experimental data.

Typical angular distributions are shown in Fig. 10 for five emission energies (55, 105, 155, 205, 255, and 305 MeV) from the 392-MeV proton-induced reactions on ^{51}V and ^{208}Pb. Although Eq. (10) is specified in the c.m. system, the experimental data are presented in the laboratory coordinate system. Overall, there is fairly good agreement. However, the calculated values tend to drop more slowly than the experimental cross-sections at higher emission energies. This discrepancy indicates that the slope parameter a of Eq. (10) needs to be refined.

To investigate the target mass dependence of the QFS contribution for the entire process, we calculated the angle-integrated cross-sections. The results for 392-MeV protons on ^{12}C, ^{51}V, and ^{208}Pb reactions are shown in Fig. 11.

Here, the MSD part of the angle-integrated cross sections was obtained as a resultant fitting normalization factor of Eq. (10) as a function of proton emission energy. The displayed result for ^{12}C was derived from the same procedure as the present experimental data, which are taken from Ref. [4]. As shown in Fig. 11, the QFS contribution increases with decreasing target mass and increasing emission energy.

V. CONCLUSION

Proton-production DDXs for 300- and 392-MeV protons induced reactions on O, V, Tb, Ta, Au, Pb, and Bi. Emitted proton energies were measured by stacked GSO(Ce) spectrometers using the $\Delta E - E$ technique. The experimental results were compared with the INC model and the QMD model. Although both models could reproduce spectral DDXs, there was a difference at the most forward and backward angles. The cause of these differences was discussed in terms of the refraction owing to the nuclear potential. Angular distributions of the present data were well accounted for by Kalbach systematics plus INC one-step calculations, and the ratios of the quasifree component to the MSD component were discussed.

ACKNOWLEDGMENTS

The authors would like to thank Professor K. Hatanaka and the RCNP cyclotron crews for their assistance in this research. This work was supported by a Grant-in-Aid for Japan Society for the Promotion of Science (JSPS) Fellows (No. 20-2608).

[1] R. E. L. Green, R. G. Korteling, J. M. D'Auria, K. P. Jackson, and R. L. Helmer, Phys. Rev. C **35**, 1341 (1987).
[2] H. Machner *et al.*, Phys. Rev. C **73**, 044606 (2006).
[3] D. S. Ginger, K. Kwiatkowski, G. Wang, W.-c. Hsi, S. Hudan, E. Cornell, R. T. de Souza, V. E. Viola, and R. G. Korteling, Phys. Rev. C **78**, 034601 (2008).
[4] T. Kin *et al.*, Phys. Rev. C **72**, 014606 (2005).
[5] J. Aichelin, Phys. Rep. **202**, 233 (1991).
[6] K. Niita, S. Chiba, T. Maruyama, T. Maruyama, H. Takada, T. Fukahori, Y. Nakahara, and A. Iwamoto, Phys. Rev. C **52**, 2620 (1995).
[7] A. A. Cowley, S. V. Förtsch, J. J. Lawrie, D. M. Whittal, F. D. Smit, and J. V. Pilcher, Z. Phys. A **336**, 189 (1990).
[8] C. Kalbach, Phys. Rev. C **37**, 2350 (1988).
[9] F. Saiho, T. Kin, S. Hohara, Y. Yamashita, M. Imamura, G. Wakabayashi, N. Ikeda, Y. Uozumi, M. Matoba, and N. Koori, Nucl. Instrum. Methods Phys. Res. A **537**, 594 (2005).
[10] H. Yoshida *et al.*, Nucl. Instrum. Methods Phys. Res. A **411**, 46 (1998).
[11] M. Makino, R. Eisberg, D. Ingham, and C. Waddell, Nucl. Instrum. Methods **81**, 125 (1970).
[12] H. W. Bertini, Phys. Rev. **131**, 1801 (1963).
[13] Y. Yariv and Z. Fraenkel, Phys. Rev. C **20**, 2227 (1979).
[14] S. G. Mashnik, Nucl. Phys. A **568**, 703 (1994).
[15] J. Cugnon, C. Volant, and S. Vuillier, Nucl. Phys. A **620**, 475 (1997).
[16] H. Duarte, Phys. Rev. C **75**, 024611 (2007).
[17] H. Iwase, K. Niita, and T. Nakamura, J. Nucl. Sci. Technol. **39**, 1142 (2002).
[18] J. W. Negele, Phys. Rev. C **1**, 1260 (1970).
[19] J. Cugnon, D. L'Hote, and J. Vandermeulen, Nucl. Instrum. Methods Phys. Res. B **111**, 215 (1996).
[20] S. Chiba, M. B. Chadwick, K. Niita, T. Maruyama, T. Maruyama, and A. Iwamoto, Phys. Rev. C **53**, 1824 (1996).
[21] V. Comparat, R. Frascaria, N. Marty, M. Morlet, and A Willis, Nucl. Phys. A **221**, 403 (1974).
[22] D. J. Horen *et al.*, Phys. Rev. C **31**, 2049 (1985).
[23] S. V. Förtsch, A. A. Cowley, J. J. Lawrie, D. M. Whittal, J. V. Pilcher, and F. D. Smit, Phys. Rev. C **43**, 691 (1991).
[24] N. S. Chant and P. G. Roos, Phys. Rev. C **15**, 57 (1977).